Measurement of Electron−Electron Interactions and Correlations Using Two-Dimensional Electronic Double-Quantum Coherence Spectroscopy

Jeongho Kim, Vanessa M. Huxter, Carles Curutchet, and Gregory D. Scholes*

Department of Chemistry, Institute for Optical Sciences and Centre for Quantum Information and Quantum Control, University of Toronto, 80 St. George Street, Toronto, Ontario M5S 3H6, Canada

Received: July 30, 2009; Revised Manuscript Received: September 23, 2009

A two-dimensional (2D) optical coherent spectroscopy that correlates the double excited electronic states to constituent single excited states is described. The technique, termed two-dimensional double-quantum coherence spectroscopy (2D-DQCS), makes use of multiple, time-ordered ultrashort coherent optical pulses to create double and single quantum coherences over the time intervals between the pulses. The resulting 2D electronic spectra map out the energy correlation between the first excited state and two-photon-allowed double-quantum states. Measurements of organic dye molecules show that the near-resonant energy offset for adding a second electronic excitation to the system relative to the first excitation is on the order of tens of millielectronvolts. Simulations of DQC spectra show that vibronic transitions add rich features to the 2D spectra. The results of quantum chemical calculations on model systems provide insight into the many-body origin of the energy shift measured in the experiment. These results demonstrate the potential of 2D-DQCS for elucidating quantitative information about electron−electron interactions, many-electron wave functions, and electron correlation in electronic excited states and excitons.

1. Introduction

Mean-field models in chemistry, that is, theories based on orbital energies, symmetries, and shape, have proven to be enormously successful for predicting structure, explaining reactivity, and qualitatively describing spectroscopy. Nonetheless, the correlated motions of electrons in molecules are very significant and may one day be harnessed to expose new modes of chemical reactivity. The goal of our work is to begin to elucidate insights into chemistry beyond mean-field approximations. To this end, an experimental framework that will test and inspire theory needs to be established. In the present report we describe the application and interpretation of a coherent two-dimensional electronic spectroscopy that measures changes in the electronic interactions among electrons and their many-body correlated response to optical excitation.

Recent advances in multidimensional coherent spectroscopy have allowed researchers to gain insights into the mechanism of excited state processes, going beyond the simple excited state decay kinetics traditionally probed by ultrafast spectroscopy.[1−11] As an optical analogue of well-developed multidimensional nuclear magnetic resonance (NMR) techniques,[12] coherent multidimensional optical spectroscopy has been used to probe the evolution of excitations and couplings between multiple chromophores absorbing at visible or infrared frequencies with femtosecond time resolution. Recent studies have reported the theory and experimental demonstration of a different two-dimensional (2D) optical coherent spectroscopy that correlates the double excited electronic states to constituent single excited states.[13−16] The technique, termed two-dimensional double-quantum coherence spectroscopy (2D-DQCS), makes use of multiple, time-ordered ultrashort coherent optical pulses to create double- and single-quantum coherences over time intervals between the pulses. This experiment is analogous to conceptually related two-dimensional NMR[17] and infrared[18] double-quantum echo spectroscopies that respectively probe spin−spin interactions and anharmonicity of molecular vibrations. The two-dimensional electronic spectrum maps the energy correlation between the first excited state and two-photon allowed double-quantum states. The principle of the experiment is that when the energy of the double-quantum state, viewed in simple models as a double HOMO-to-LUMO excitation, equals twice that of a single excitation, then no signal is radiated. However, electron−electron interactions—a combination of exchange interactions and electron correlation—in real systems[19] generates a signal that reveals precisely how the energy of the double-quantum resonance differs from twice the single-quantum resonance. The energy shift measured in this experiment reports how the second excitation is perturbed by both the presence of the first excitation and the way that the other electrons in the system have responded to the presence of that first excitation.

In the first experimental demonstration of 2D-DQCS,[15] we compared a series of organic dye molecules. We found that the measured 2D-DQC spectra were qualitatively consistent with the prediction for an ideal system wherein electron correlation produces a strong peak and an oppositely signed mirror image symmetrically arranged either side of the diagonal, where the single coherence frequency equals approximately half the double coherence frequency. However, it is evident that the signals contained richer information than that predicted by the purely electronic model.[13,14] We have now included vibronic progressions and corresponding Franck−Condon overlaps into the expression for predicting the 2D-DQC spectra. Here we report the experimental demonstration of the 2D-DQCS with details not presented in the previous work[15] and extended results on the dependence of 2D-DQC spectra on the solvent and excitation wavelengths. In addition, we present simulations of how vibrational modes of different frequency contribute to the 2D-DQC spectra, showing that consideration of the vibrations enables us to successfully simulate the experimental data.

---

* Corresponding author, gscholes@chem.utoronto.ca.

10.1021/jp907327m CCC: $40.75

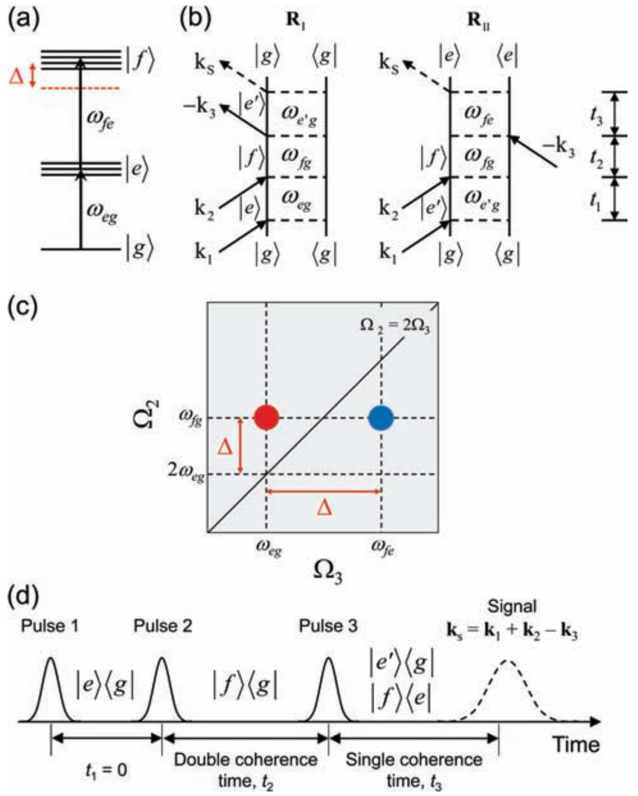

Figure 1. (a) A three-level system consisting of ground (g) and manifolds of single (e) and double (f) excited states. The red dotted energy level has an energy of exactly twice the $g \rightarrow e$ transition frequency, i.e., $2\omega_{eg}$. The difference Δ between ω_{fg} and $2\omega_{eg}$ represents the anharmonicity of the electronic oscillator arising from the electron correlation. (b) Feynman diagrams for two quantum pathways $\mathbf{R}_I$ and $\mathbf{R}_{II}$ contributing to the 2D-DQC signal. The two quantum pathways interfere in a way that allows mapping of the energies of single and double excited states in a 2D frequency space. (c) Ideal representation of 2D-DQC spectrum for the simplest three-level system. See text. (d) A sequence of three coherent pulses used in the 2D-DQCS.

2. Theory of 2D-DQCS

The 2D-DQCS experiment employs a sequence of three interactions between the system and ultrashort laser pulses, followed by interferometric detection of the third-order nonlinear optical signal radiated in the $\mathbf{k}_s = \mathbf{k}_1 + \mathbf{k}_2 - \mathbf{k}_3$ phase-matched signal direction, as shown schematically in Figure 1. The first two light−matter interactions, which are instigated in our experiment by two ultrashort laser pulses that arrive simultaneously at the sample, promote the system to the double-quantum coherence. Double quantum coherence means a superposition state of the electronic ground and double-excitation states. The third pulse interacts with the double-quantum coherence to generate the signal. The basic expression for the response function is[14]

$$S(\Omega_3, \Omega_2, t_1 = 0) = S_{\mathrm{I}} - S_{\mathrm{II}} = \sum_{e,e',f} \frac{\mu_{fe}\mu_{eg}}{\Omega_2 - \omega_{fg} + i\gamma} \times \left[\frac{\mu_{fe'}\mu_{e'g}}{\Omega_3 - \omega_{e'g} + i\gamma} - \frac{\mu_{ge'}\mu_{e'f}}{\Omega_3 - \omega_{fe'} + i\gamma}\right] \quad (1)$$

where $\omega_{\alpha\beta}$ is the electronic transition frequency between states labeled α and β, $\mu_{\alpha\beta}$ is the corresponding transition dipole magnitude, and γ is a phenomenological damping constant. In our calculations we model these terms as Gaussian functions rather than Lorentzians and include correlated static disorder in the transition frequencies as described previously.[15] $|g\rangle$ is the ground state, while $|e\rangle$, $|e'\rangle$, and $|f\rangle$ are states from the manifolds of single-quantum states and double-quantum states, respectively, that can be accessed by our excitation conditions, Figure 1a. A single-quantum state is one-photon allowed and a double-quantum state is two-photon allowed. Equation 1 suggests an infinite temperature approximation for the solvent bath, which is usually a poor approximation for solution phase spectroscopy of molecules because it does not predict, for example, the dynamic Stokes shift. However, DQCS involves only short (relative to the time scales of solvent relaxation) coherence time intervals and no population time. Therefore it is reasonable to expect the results will be insensitive to details of solvation that might otherwise influence $\omega_{\alpha\beta}$. We show in section 4C that this is the case.

The important point regarding this experiment is that there are two pathways by which a signal can be produced, represented by the Feynman diagrams shown in Figure 1b. These pathways share the common term $1/(\Omega_2 - \omega_{fg})$, and thus the energies of double-quantum resonances, ω_{fg}, are projected along the Ω_2 axis of the 2D spectrum. The two terms in parentheses are the contributions that differentiate the two signal pathways, and it can be seen that they have opposite signs, that is, they are π out-of-phase. These pathways contribute differently to the signal along the Ω_3 axis, which results in their interference. The first pathway gives the energies of single-quantum resonances between ground and single excited states, i.e., $\Omega_3 = \omega_{e'g}$, while the second reveals resonances between double and single excited states, $\Omega_3 = \omega_{fe}$. Thus, 2D-DQCS correlates the energies of double-quantum resonances, ω_{fg}, to those of single-quantum resonances, $\omega_{e'g}$, and ω_{fe}, in a 2D spectrum. This correlation becomes clear in the ideal representation of a 2D-DQC spectrum illustrated in Figure 1c. The Ω_3 axis represents the single excitation frequency, while the Ω_2 axis corresponds to the double excitation frequency. Along the Ω_3 axis, positive (red) and negative (blue) peaks are located at the frequencies of ω_{eg} and ω_{fe}, respectively. Along the Ω_2 axis, both peaks are placed at the common double-quantum resonance energy, ω_{fg}. The diagonal line, $\Omega_3 = 2\Omega_3$, represents the case when the double-quantum energy is exactly twice the single-quantum energy, that is, $\omega_{fg} = 2\omega_{eg}$ and thus $\omega_{fe} = \omega_{eg}$. Therefore, the difference between a peak and the diagonal along the Ω_2 axis or between the two peaks along the Ω_3 axis corresponds to the anharmonicity Δ of the electronic oscillator arising from electron correlation. Some comments on the meaning of Δ are provided in section 7.

As shown above, the two quantum pathways interfere in a unique way so that the two destructively interfering terms are not canceled out in the presence of electron correlation. The way that those two pathways interfere to generate the 2D-DQC signal is similar in its origin to the dephasing-induced resonances observed with various other nonlinear spectroscopies. For example, in third-order coherent Raman spectroscopy,[20,21] terms involving ground and excited state populations are imperfectly canceled by introduction of pure dephasing, leading to a new Raman resonance. Also, similar interference effects form a basis for the signal generation in fifth-order polarizability response spectroscopy[22] and second-order difference frequency generation spectroscopy.[23]

The time ordering of the sequence of three ultrashort laser pulses is shown in Figure 1d. Pulse 1 interacts with the system to create a coherence between $|g\rangle$ and $|e\rangle$. Simultaneously (in our experimental configuration), pulse 2 interacts with the system to produce an electronic coherence between $|g\rangle$ and $|f\rangle$, that is, the double-quantum coherence represented by the off-diagonal density matrix element $\rho_{fg} = |f\rangle\langle g|$. After a double coherence time delay, t_2, the system interacts with pulse 3, which induces either the single-quantum coherence $|e'\rangle\langle g|$ or $|f\rangle\langle e|$. During a time period, t_3, termed the "single coherence time", the third-order polarization $P^{(3)}$ is radiated in the direction $\mathbf{k}_s = \mathbf{k}_1 + \mathbf{k}_2 - \mathbf{k}_3$, where $\mathbf{k}_1$, $\mathbf{k}_2$, and $\mathbf{k}_3$ are wave vectors of pulses 1, 2, and 3, respectively. 2D Fourier transformation of $P^{(3)}(t_2,t_3)$with respect to t_2 and t_3 delivers 2D spectra as a function of two frequency axes, Ω_2 and Ω_3, which are conjugates to t_2 and t_3, respectively. In practice, $P^{(3)}(t_2,\Omega_3)$ is directly obtained using a combination of spectrograph and CCD array detector. Since one frequency axis is already obtained by a dispersed detection scheme, only Fourier transformation along the t_2 delay is needed to produce a 2D spectrum as a function of Ω_2 and Ω_3

$$S(t_1 = 0, \Omega_2, \Omega_3) = \int_{-\infty}^{\infty} P^{(3)}(t_2, \Omega_3) \exp(i\Omega_2 t_2)\, \mathrm{d}t_2 \tag{2}$$

Quantum chemical calculations can be used to estimate the parameters needed to illustrate model 2D-DQC spectra based on eq 1. Some technical discussion and interpretation of the information content in 2D-DQC data in the context of state-of-the-art quantum chemical calculations is given in section 7. Here we aim to introduce the concepts.

A quantum chemical method suited to illustrate the 2D-DQC spectra for large molecules is the symmetry adapted cluster configuration interaction (SAC-CI) method developed by Nakatsuji and co-workers.[24] The SAC-CI method allows for a balanced treatment of electron correlation effects both on the ground and on the excited states through consideration of single and double excitations (SD-R version). This method provides an important electron correlation correction, for example, compared to the CI-singles method, in which the excited states are described roughly with a Hartree−Fock quality. Equally important for the description of 2D-DQCS data, the SAC-CI method treats both single and double excited states on an equal footing. Therefore, we have performed SAC-CI SD-R/6-31G calculations on geometries optimized at the MP2/6-31G(d) level of theory for different molecules. Such calculations were performed using the *LevelOne* thresholds for selection of double excitation operators, as implemented in the Gaussian 03 code.[25] We note here that further inclusion of higher-order, e.g., triple and quadruple, excitations are expected to lead to more significant corrections to the energies of double excited states,[26] but this would be computationally too expensive for the systems we considered.

Examples of 2D-DQCS maps over a broad energy range for three five-ring polyacene molecules, pentacene, dibenz[*a*,*h*]anthracene, and dibenz[*a*,*c*]anthracene, calculated using eq 1 and the SAC−CI quantum chemical method, are shown in Figure 2. The structures of the molecules are drawn in Figure 2a. According to this quantum chemical method, there are 41 electronic states for dibenz[*a*,*h*]anthracene that lie below 9 eV. Of these, eight can be optically excited from the lowest energy singlet excited state, and they are listed on the right side of Figure 2b. Red peaks are contributed by the pathway $\mathbf{R}_\mathrm{I}$ and blue troughs (negative peaks) come from $\mathbf{R}_\mathrm{II}$. The blue and red peaks are displaced symmetrically along the Ω_3 axis about the diagonal $\omega_{fe} = \omega_{eg}$. These features map out the energies of the $|f\rangle$ states relative to $|e\rangle$. Calculated DQC spectra for three polyacene molecules are compared in Figure 2c−e. It is evident that the transition energies as well as the transition dipole strengths for these states depend on the molecular structure. In particular, as the symmetry of the molecule increases, the number of features in the DQC spectrum decreases.

How should we interpret the DQC spectra? If the total energy of a molecular wave function were determined simply by integrals between the average electron density of electrons, then mean-field treatments, like the Hartree−Fock method, would yield accurate descriptions of electronic structure. In that case, all the information would be carried by the orbital representation of a molecule and electronic transition energies would be the energy gaps between occupied and unoccupied orbitals (although, for the sake of rigor, note that only the energies of occupied orbitals are found using the Hartree−Fock procedure). In this picture, for every single excitation of an electron from an occupied to unoccupied orbital there will be a corresponding double-excitation of precisely twice the energy. At this primitive level of theory, therefore, there will be no DQC signal from the double excitation of HOMO to LUMO because pathways $\mathbf{R}_\mathrm{I}$ and $\mathbf{R}_\mathrm{II}$ exactly cancel. However, the second field-matter excitation in the experiment can promote various other symmetry-allowed occupied to unoccupied orbital transitions, which will invariably have different energies than the first excitation. These transitions will produce DQC signals when referenced to the first excitation, and the resulting pattern in the DQC spectrum would qualitatively resemble the plot shown in Figure 2b (note, however, that the DQC spectra in Figure 2 were calculated using the more advanced approach described above).

At the next level of approximation we consider electron−hole exchange, that is, there are two distinct ways of promoting an electron from an occupied to unoccupied orbital because a closed shell orbital contains two spin-paired electrons. The properly symmetrized excited singlet state is raised in energy by the exchange interaction (half the singlet−triplet splitting) compared to the orbital energy difference. The double excitation, however, is a closed shell state and is not raised in energy by the electron−hole exchange. Hence the transition energy ω_{fe} should be red-shifted by the singlet−triplet splitting (several hundred millielectronvolts for molecules) compared to ω_{eg} at this level of theory. It therefore makes sense that other states of appropriate symmetry (cf. the pattern of states in Figure 2b) may lie closer in energy to $2\omega_{eg}$ than the double-quantum state (we refer to the HOMO to LUMO double excitation as the double-quantum transition). This is a key point and it is examined further in section 7.

Finally we need to account for the fact that the occupied to virtual orbital excitations produce configurations that interact with each other. Hence the correct eigenstates of the system are obtained by diagonalizing this matrix, known as full configuration interaction (CI). Part of the improvement obtained here is that it allows the unoccupied orbitals obtained at the Hartree−Fock level to relax, which, strictly speaking, provides a mean-field correction to the models discussed above. For example, this is what is captured in CI singles. There will also be mixing among single excitations and double excitations, etc. that substantially modify our interpretation of the DQC spectra. These effects give the electron correlation energy differences among the three states that we probe. Physically, the electron correlation energy accounts for ways that electrons avoid each other, by correlating their motions to minimize Coulomb repulsions. The motivation behind our experiments is to develop an experimental probe of how the electron correlation energy

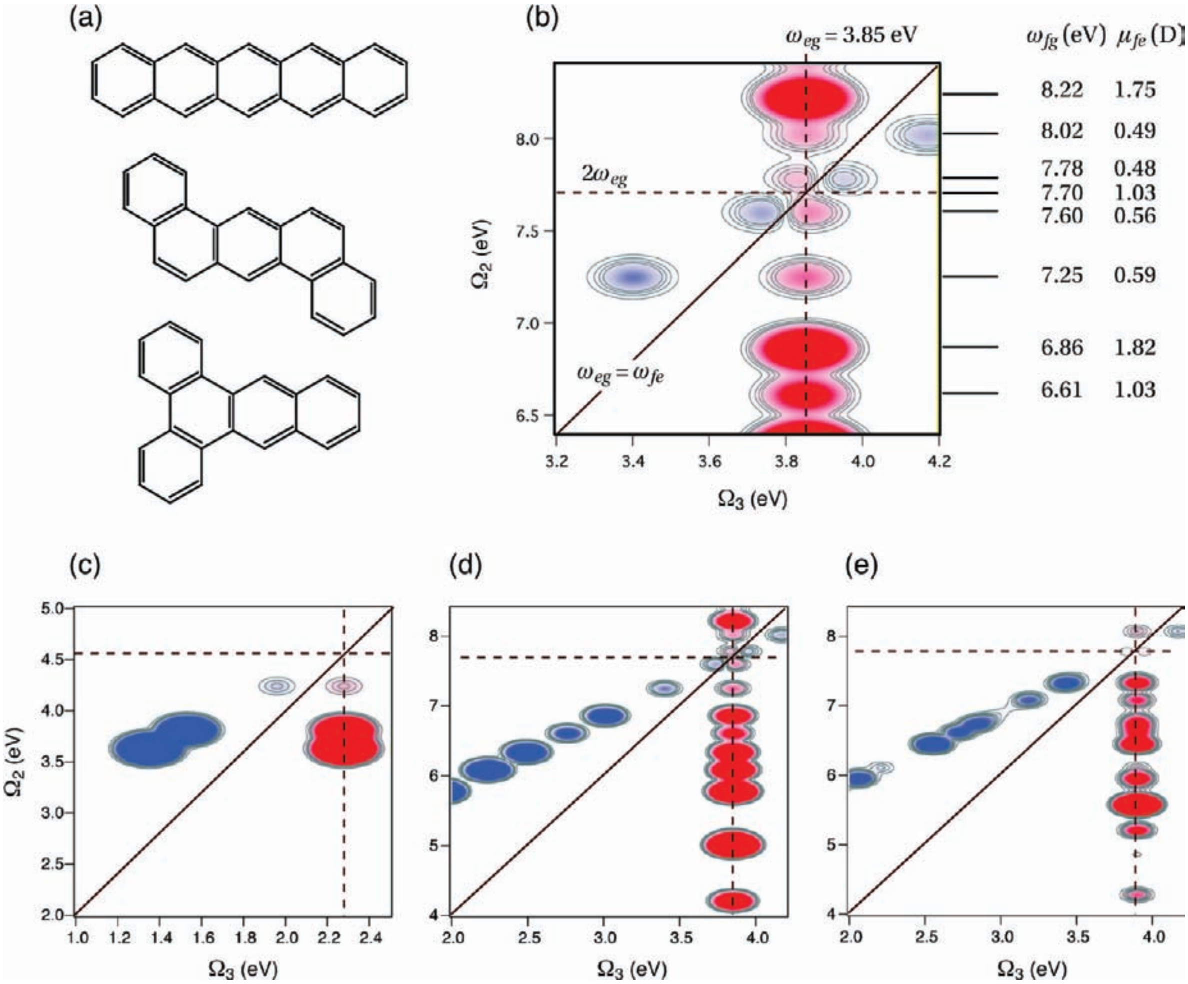

Figure 2. (a) Structures of pentacene, dibenz[*a*,*h*]anthracene, and dibenz[*a*,*c*]anthracene. (b) Detailed plot of the 2D-DQC spectrum calculated for dibenz[*a*,*h*]anthracene (see text for details). (c−e) 2D-DQC spectra calculated for pentacene, dibenz[*a*,*h*]anthracene, and dibenz[*a*,*c*]anthracene, respectively. The diagonal lines specify $2\Omega_3 = \Omega_2$. The dashed vertical lines show $\Omega_3 = \omega_{eg}$, while the dashed horizontal lines indicate $\Omega_2 = 2\omega_{eg}$.

changes between the ground state, single excited state, and double quantum states.

3. Experimental Section

A. Setup. The details of the laser setup are described elsewhere.[27] Briefly, coherent optical pulses with 130 fs pulse duration and 800 μJ pulse energy at 775 nm center wavelength were generated from a 1 kHz repetition rate Ti:sapphire amplified laser (Clark-MXR, CPA-2001). They were converted into light tunable from 450 to 650 nm by a noncollinear optical parametric amplifier (NOPA). The NOPA output pulses were sent to a pair of quartz prisms for precompensation of optics material dispersion and split by a beamsplitter into two beams. The intensities of the two beams were controlled by a combination of half-wave plate and polarizer inserted into each beam.

The 2D-DQCS measurement was implemented using an inherently phase-stabilized experimental setup using a diffractive optic (DO), based on the design by Miller and co-workers.[28] High accuracy of phase stability is critical for implementing 2D-DQCS in the visible frequencies because fluctuations in path length of each beam lead to a higher phase error in this spectral region than in the infrared. The schematic of the setup is shown in Figure 3. The two beams split by the beamsplitter were focused and spatially overlapped on the DO with a 25 cm focal length lens to give a pair of replicas at ±1 diffraction orders for each beam. The DO was designed for highly efficient ±1 order diffraction with 70% diffraction efficiency. The resulting four beams (with the light of all other diffraction orders blocked by a mask) were achromatically collimated and focused into the sample by a pair of 25 cm focal length paraboloid mirrors. The pulses were characterized by transient grating frequency-resolved optical gating (TG-FROG) of pure solvent (ethanol). Near-transform-limited pulses were obtained with a pulse duration of 18−22 fs at the sample position, depending on the wavelength, and a time bandwidth product of ∼0.47.

In 2D-DQCS, the introduction of time delays between the pulses with suboptical period precision is required to perform a Fourier transform without artifacts. Such precise control of time delays is achieved by using pairs of movable glass wedges (1.5 mm thickness, 1° wedge angle, fused silica) inserted into E_1, E_2, and E_3 beams, as was introduced by Fleming and co-workers.[9] Each wedge is paired with an identical second one at an antiparallel orientation. By laterally translating one wedge of the pair along the direction of inner surface, the wedge pair serves as one glass plate of varying thickness without any beam displacement. In our setup, one wedge of the pair was mounted on a computer-controlled dc motor translational stage (Newport, MFA-CC) with 100 nm motion resolution, yielding precise time delays of ∼2.7 as precision over a total travel range of ∼500 fs. Each time delay using wedge pairs was calibrated using spectral interferometry, as is done for the 2D photon echo experiment.[9,29] Briefly, spectral interferograms, which are gener-

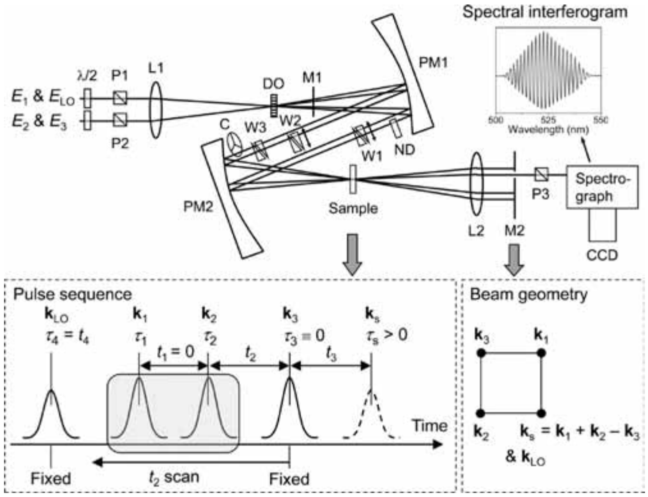

Figure 3. Experimental setup for 2D-DQCS. Two optical pulses, whose intensities are adjusted by half-wave plates ($\lambda/2$) and polarizers (P1, P2), are focused on a diffractive optic (DO) by a 25 cm focal length achromatic lens (L1) to generate four optical pulses, E_1, E_2, E_3, and E_{LO}, diffracted at first order. The four beams transmitted through the mask (M1) are collimated and focused onto the sample by a pair of 25 cm focal length paraboloid mirrors (PM1, PM2). The time delays between the pulses, t_1, t_2, and t_3, are varied with interferometric precision by moving one of each glass wedge pair (W1, W2, and W3) inserted into the E_1, E_2, and E_3 optical beams. The E_1, E_2, E_3, and E_{LO} pulses are incident on the sample with $\mathbf{k}_1$, $\mathbf{k}_2$, $\mathbf{k}_3$, and $\mathbf{k}_{LO}$ wavevectors at τ_1, τ_2, τ_3, and τ_4 arrival times, respectively. Time zero is defined at the center of pulse 3, i.e., $\tau_3 = 0$. The third-order signal ($\mathbf{k}_s$) is radiated in the direction of $\mathbf{k}_1 + \mathbf{k}_2 - \mathbf{k}_3$, the same direction as $\mathbf{k}_{LO}$ in the four-beam boxcars geometry. The LO pulse is attenuated by a neutral density filter (ND) and always precedes all other three pulses by the time delay, t_4, that was set to be $t_4 = \tau_4 = -500$ fs. After being collimated by a 25 cm focal length lens (L2), the heterodyned signal is detected as a spectral interferogram along the Ω_3 axis by a combination of spectrograph and CCD array detector.

ated from diffraction of a pair of laser beams (for example, E_1 and E_2) through a pinhole placed at the sample position, were recorded while scanning the position of a wedge in 5 μm steps. The measured spectral interferograms along the wedge translation gives temporal oscillations at each wavelength. By counting the number of optical periods for a particular wavelength over the scanned distance, a calibration factor for conversion of wedge position into time delay was calculated for each wedge pair.

When the three pulses interact with the sample, the third-order signal is radiated in the $\mathbf{k}_s = \mathbf{k}_1 + \mathbf{k}_2 - \mathbf{k}_3$ direction, which coincides with the propagation direction of the fourth beam, denoted the local oscillator (LO), in the four-beam boxcars geometry. As a result, the signal electric field is mixed with the LO field to yield the heterodyned signal. The heterodyned signal is linear (instead of quadratic) in the induced third-order polarization and allows phase-sensitive detection of the real and imaginary parts of the third-order polarization. In addition, heterodyne detection provides the advantage of amplifying weak signals proportional to the amplitude of the LO field, yielding a superb signal-to-noise ratio. The DO enables passively phase-locked heterodyne detection with excellent phase stability by ensuring well-matched phase fronts of the pulses and automatic spatial overlapping of the signal and LO fields. The heterodyned signal is dispersed with 1200 grooves/mm grating (blazed at 500 nm) in a 0.63 m spectrograph (Andor, SR-163) on a 1600 × 400 pixel, thermoelectrically cooled charge-coupled device (CCD) array detector (Andor, Newton DU971N), yielding the Fourier transformation with respect to the t_3 time delay.

A notable feature of our approach is that we use the usual phase-locked pulse pairs generated by the DO, rather than requiring fully phase-locked pulses. The reason that this works successfully for the DQC experiment is that we use a scan sequence isomorphic to that used in "normal" 2D photon echo spectroscopy, where the signal arrives in the $\mathbf{k}_{PE} = -\mathbf{k}_1 + \mathbf{k}_2 + \mathbf{k}_3$ direction and the pulse pairs E_1/E_2 and E_3/E_{LO} are inherently phase-locked. In this case, the phase of the DO-based setup is stabilized because fluctuations in phase of the four pulses cancel out between phase-locked pulse pairs, i.e., $(\varphi_2 - \varphi_1) + (\varphi_3 - \varphi_{LO}) = 0$. For the DQC experiment we use the same four-beam configuration,[30] but we relabel $E_1 \leftrightarrow E_3$. In this case, the signal is radiated in the new direction of $\mathbf{k}_{DQC} = \mathbf{k}_1 + \mathbf{k}_2 - \mathbf{k}_3$ and the E_3/E_2 and E_1/E_{LO} pulse pairs are locked in phase. The phase stability of the third-order signal is still maintained consistently with the phase matching condition of the DQC experiment by simply relabeling the pulses 1 and 3, i.e., $(\varphi_2 - \varphi_3) + (\varphi_1 - \varphi_{LO}) = 0$. Therefore, the inherent phase stability achieved by the DO-based setup also applies to the 2D-DQCS experiment.

B. Data Acquisition and Evaluation. Characterization of the heterodyned third-order signal field is achieved by spectral interferometry[31] with the LO field. The LO pulse precedes pulse 3 by the time delay, t_4, which was set to be about -500 fs in our measurements. This leads to a spectral interference pattern, as shown in the inset of Figure 3, with its fringe spacing along the Ω_3 axis determined by the time delay, t_4

$$I_{het}(\Omega_3) = |E_s(\Omega_3) + E_{LO}(\Omega_3)\exp(i\Omega_3 t_4)|^2 \tag{3}$$

This spectral interferogram contains the full information needed to retrieve both the amplitude and phase of the third-order signal versus Ω_3, yielding an effective Fourier transform with respect to the time delay, t_3. From the measured spectral interferogram, the complex cross term of eq 3 is obtained as[31-33]

$$I_f(\Omega_3) = \sqrt{I_s(\Omega_3)I_{LO}(\Omega_3)}\exp\{i[\varphi_s(\Omega_3) - \varphi_{LO}(\Omega_3) - \Omega_3 t_4]\} \tag{4}$$

where $\varphi_s(\Omega_3)$ and $\varphi_{LO}(\Omega_3)$ are the phases of signal and LO fields, respectively. Both the signal intensity, $I_s(\Omega_3)$, and phase, $\varphi_s(\Omega_3)$, of the heterodyne detected signal are recovered by dividing eq 4 by $(I_{LO}(\Omega_3))^{1/2}$ and $\exp\{-i[\varphi_{LO}(\Omega_3) + \Omega_3 t_4]\}$. The LO intensity, $I_{LO}(\Omega_3)$, is obtained from a LO spectrum measured with pulses 1−3 blocked, and the time delay t_4 is retrieved from the Fourier transform of an interference spectrum between pulse 3 and the LO pulse. The phase of the LO field, $\varphi_{LO}(\Omega_3)$, is calibrated using a separately measured spectrally resolved pump−probe spectrum,[7,9] as discussed below.

A series of spectral interferograms were recorded as the double coherence time t_2 was scanned, yielding the raw 2D data in terms of t_2 and Ω_3. The t_2 delay was scanned by simultaneously moving both pulses 1 and 2 so that the t_4 delay between the LO pulse and pulse 3 is kept constant for spectral interferometry. The data were collected only at $t_2 \geq 0$ until the double-quantum coherence dephases completely, typically within 100 fs. This is in contrast to 2D photon echo spectroscopy (2D-PES), where both positive and negative single coherence time values constituting two conjugate quantum pathways are scanned. In terms of time ordering of the pulses, 2D-DQCS can be considered as "reverse photon echo" spectroscopy because the two pulses first interact with the system followed by a third pulse, which is a reversed pulse ordering compared to 2D-PES.[18,34−39]

By numerically Fourier transforming the measured signal with respect to t_2,[7] the 2D-DQC spectra correlating the double-quantum (Ω_2) and single-quantum (Ω_3) resonances are generated. The t_2 scan was made in 0.1 fs time steps to ensure sufficient sampling rate for the double quantum resonance frequencies of the measured samples. In addition, a short time step was required to retrieve a flat phase profile along the t_2 axis in the Fourier transform procedure, which is important in obtaining accurate Ω_2 energies. See Supporting Information for details.

We found that the calibration of the wedge translation is crucial for determining accurate Ω_2 energies in the processed 2D-DQC spectra. In other words, an error in the delay calibration factor of the wedges inserted in pulses 1 and 2 causes an error in scaling along the t_2 axis and thus a shift of the observed Ω_2 energy. For example, only a 1% error in the calibration factor for the double-quantum resonance energy, which was on the order of ~4 eV for the systems studied in this work, results in a ~40 meV shift of the peak position along the Ω_2 axis. However, even with the precise wedge calibration procedure using spectral interferometry, an error of ±0.5% in the delay calibration factor was unavoidable in our setup. In addition to the wedge calibration error, the slope of the phase surface along the t_2 axis also sensitively affects the Ω_2 energy. Although only a flat region of the phase surface was carefully selected and extrapolated to obtain the Ω_2 axis by a Fourier transform, the phase retrieval procedure still remains a source of error in determining the Ω_2 energy. To compensate for those errors that can arise from delay calibration and/or Fourier transform procedure, we calibrated the Ω_2 axis by ensuring the positions of the major positive and negative peaks in the 2D-DQC spectra of organic dye molecules were symmetric with respect to the diagonal line, based on the theoretical prediction. Such a procedure does not affect the measured electron correlation energy in the 2D-DQC spectra since the entire peak features are shifted together only along the Ω_2 axis with their relative positions intact.

The 2D-DQC spectra are complex quantities with both amplitude and phase. In this paper, we present the real part (Re) and absolute value (Abs) of the spectra. The former represents the absorptive contribution of the third-order polarization, while the latter includes both absorption and refractive index contributions. For the phasing of the 2D-DQC spectra, we invoke the projection-slice identity,[7,40] which states that the one-dimensional projection of the 2D spectrum $S(\Omega_2, \Omega_3)$ onto a line (Ω_3 axis in this case)

$$P_{2D}(\Omega_3) = \int_{-\infty}^{\infty} S(\Omega_2, \Omega_3)\, d\Omega_2 \tag{5}$$

is equal to the Fourier transform of the one-dimensional slice through the origin of 2D time-domain signal $S(t_2, t_3)$ parallel to the projection line (along the t_3 axis in this case)

$$s(t_2 = 0, \Omega_3) = \int_{-\infty}^{\infty} S(t_2 = 0, t_3) \exp(i\Omega_3 t_3)\, dt_3 \tag{6}$$

Following this relation, the (absorptive) real part of the projection of the 2D-DQC spectrum onto the Ω_3 axis (eq 5) is equal to a separately measurable spectrally resolved pump−probe signal measured at $t_2 = 0$ (eq 6). Specifically, the pump−probe signal we measure corresponds to zero time delay between the pump and probe pulses, with the signal spectrally resolved and intrinsically heterodyned by the probe beam with the phase relationship yielding the absorptive signal. This comparison with the spectrally resolved pump−probe signal has been commonly employed in phasing strategies for 2D photon echo spectroscopy.[7,40] Here, it should be noted that, although the 2D-DQCS signal is radiated in a direction ($\mathbf{k}_s = \mathbf{k}_1 + \mathbf{k}_2 - \mathbf{k}_3$), which is different from that of the pump−probe signal ($\mathbf{k}_{PP} = \pm\mathbf{k}_1 \mp \mathbf{k}_2 + \mathbf{k}_3$), these two signals become indistinguishable at $t_2 = 0$ ($t_1 \equiv 0$ in 2D-DQCS), when all three pulses are coincident in time. Hence, to phase the 2D-DQC spectra, the LO phase, $\varphi_{LO}(\Omega_3)$, in eq 4 is adjusted so that the real part of projection of the 2D spectrum onto the Ω_3 axis matches the profile of the pump−probe spectrum that is separately measured at $t_2 = 0$.

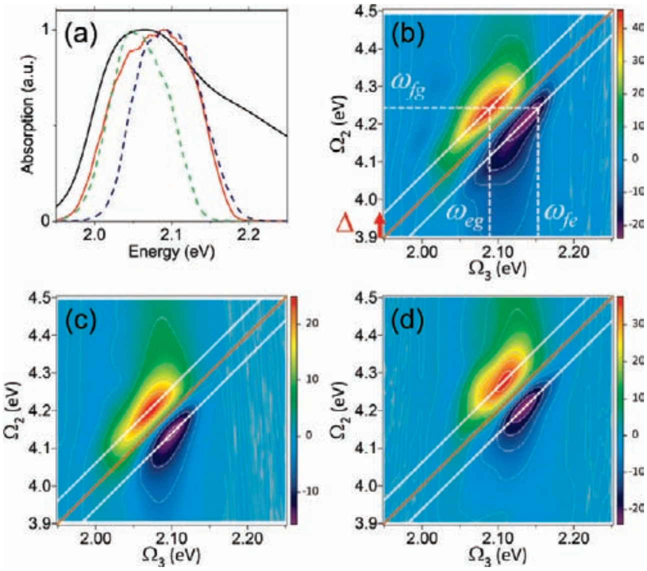

Figure 4. (a) Absorption spectrum of cresyl violet (black solid) and laser spectra of 595 nm (2.09 eV) centered, 28 nm (95 meV) fwhm bandwidth pulse (red solid), 602 nm (2.06 eV) centered, 21 nm (73 meV) fwhm bandwidth pulse (green dashed), and 590 nm (2.11 eV) centered, 20 nm (73 meV) fwhm bandwidth pulse (blue dashed). (b) The Re 2D-DQC spectrum of cresyl violet measured with the 595 nm, 28 nm bandwidth laser pulse. The diagonal line (orange) at $\Omega_2 = 2\Omega_3$ represents the double-quantum resonance energies when there is no correlation between single excitations. Two white lines are plotted in the diagonal direction to indicate the positions of major (positive and negative) peaks. The energy difference between the diagonal and any of the peaks defines the double quantum correlation energy Δ that quantifies the correlation energy between two single-quantum excitations. (c) The Re 2D-DQC spectrum of cresyl violet measured with the 602 nm, 21 nm bandwidth laser pulse. It can be seen that the negative peak lies at a lower Ω_2 energy than the positive peak. (d) The Re 2D-DQC spectrum of cresyl violet measured with the 590 nm, 20 nm bandwidth laser pulse. It can be seen that the negative peak lies at a lower Ω_2 energy than the positive peak.

In this work, results for dilute solutions of cresyl violet, Nile blue, and Nile red (aka phenoxazone 9) are presented. Cresyl violet and Nile blue were dissolved in ethanol, and Nile red was dissolved in ethanol, acetone, dicholoromethane and dimethyl sulfoxide (DMSO). The optical densities of samples were kept at ~0.3−0.4 in a 1 mm or 0.2 mm (only for cresyl violet) path length quartz cuvette. All data were recorded at room temperature.

4. Experimental Results and Discussion

A. 2D-DQC Spectra. 2D-DQC spectra measured for cresyl violet are shown in Figure 4. Since the Re spectrum exhibits narrower features, arising from isolation of the absorptive contribution, than the Abs spectrum that shows an averaged response of absorptive and refractive index contributions,[7,9] we only show the Re data. The diagonal line, $\Omega_2 = 2\Omega_3$, serves as a reference for the energies of double quantum states because it represents the case when $\omega_{fe} = \omega_{eg}$ and thus $\omega_{fg} = 2\omega_{eg}$.

As can be seen in Figure 4b, the Re 2D-DQC spectra contain two major peaks, one on the left and the other to the right of the diagonal. The two peaks have oppositely signed amplitudes, as predicted by theory.[41] As shown in the ideal 2D-DQC spectrum in the previous section, the peak position along the Ω_2 axis represents the energy of the double-quantum resonance, ω_{fg}, while the positions of the left and right peaks along the Ω_3 axis reveal the energies of the relevant single-quantum resonance, ω_{eg}, and its correlation-induced shifted resonance, ω_{fe}, respectively. Unlike the ideal case, both peaks are elongated along the diagonal, while the peak width in the antidiagonal direction is narrow and well resolved. The width of the peaks along the Ω_3 axis reflects the inhomogeneous line width of the transition from the ground state to a single excited state. The positive ω_{eg} peak is stronger than the negative ω_{fe} peak. The asymmetry of the positive and negative peaks in their amplitudes indicates that the measured 2D-DQC spectra are strongly influenced by the vibronic structure in the electronic transitions, leading to the appearance of additional cross-peaks. We have found that vibronic transitions add rich structure to the 2D-DQC data, as detailed in the next section. Another contribution to the asymmetry of the positive and negative peaks could be the difference in the dephasing rate of the two output coherences, $|e'\rangle\langle g|$ and $|f\rangle\langle e|$, corresponding to $\mathbf{R}_{\mathrm{I}}$ and $\mathbf{R}_{\mathrm{II}}$, respectively. Because the latter could dephase more rapidly than the former and therefore contribute less to the 2D-DQC signal, the negative peak is smaller in its amplitude than the positive peak.

A line passing through the maximum of the ω_{eg} peak in the diagonal direction is compared with the diagonal line to obtain the energy shift of the peak relative to the diagonal. Similarly, we can draw a line through the maximum of the ω_{fe} peak. The energy offsets along the Ω_2 axis Δ_+ and Δ_- should be the same. However, partly owing to the extreme sensitivity of Ω_2 to calibration of the t_2 delay, we often find that the peaks are not symmetrically displaced about the diagonal. Therefore, we estimate the DQC energy shift as an average: $\Delta = (\Delta_+ + \Delta_-)/2$. The DQC energy shift Δ provides a measure of correlation between two single excitations comprising a double-quantum state. Δ quantifies the change in the energy of double-quantum state (relative to double the single-quantum energy) induced by the interaction between the two single-quantum excitations. Using an analogy to vibrational oscillators,[18] Δ represents the anharmonicity of the collective electronic oscillator (quasi-particle). The Δ value along the Ω_2 axis is equal to the difference between the positions of the two peaks along the Ω_3 axis, $\omega_{fe} - \omega_{e'g}$, indicating the correlation strength between the ω_{eg} and ω_{fe} transitions. In accordance with the upshift of the ω_{eg} peak from the diagonal, the Δ values of all the organic dyes examined in this work are positive. That result is quite different than what is expected based on analogy to vibrational anharmonicity. The reason is that electronic oscillators are governed by a complicated many-body response of the electrons in the molecule. Some insight into this matter is given in section 7.

B. Effect of Laser Bandwidth and Cell Path Length on 2D-DQC Spectra. In our previous work,[15] it was seen that the Ω_2 energy of the negative ω_{fe} peak is lower than that of the positive ω_{eg} peak by tens of millielectronvolts, which is comparable to the Δ value measured for organic dyes. From further measurements in this work, it was found that such a difference in Ω_2 energy between the two peaks is mainly caused by the limited spectral bandwidth of the excitation pulse. The bandwidth dependence of 2D-DQC spectra is well demonstrated by comparing 2D-DQC spectra measured with laser pulses of broad and narrow bandwidths, shown in Figure 4b−d. In the 2D spectrum obtained with rather broad (95 meV) bandwidth pulses in Figure 4b, the positive and negative peaks lie at similar Ω_2 energies, although the negative peak is still located at a slightly lower energy. In contrast, the 2D spectra measured with narrower (73 meV) bandwidth pulses in panels c and d of Figure 4 show substantial discrepancy in Ω_2 energy between the positive and negative peaks. Such a difference arises because the narrow bandwidth of the excitation pulse limits the visible width on either the blue side of the negative peak (Figure 4c) or the red side of the positive peak (Figure 4d). When we expanded the bandwidth of the excitation pulse even further than that in Figure 4b, it was seen that the Ω_2 energies of positive and negative peaks lie at the same energy. It should be noted that the Δ value, which is the measure of correlation between single excitations, is not affected by the excitation bandwidth.

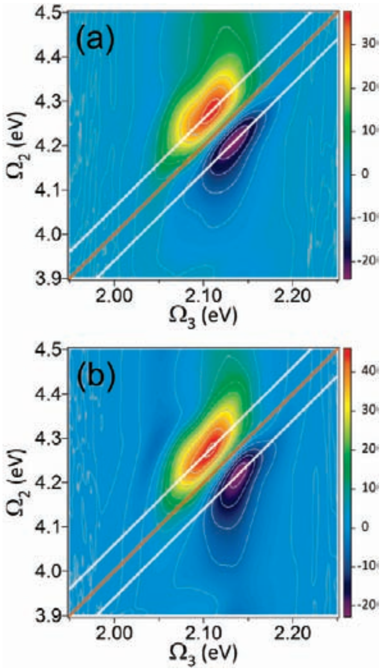

Figure 5. The Re 2D-DQC spectra of cresyl violet measured with a 590 nm, 20 nm bandwidth laser pulse in (a) 1 mm path length and (b) 0.2 mm path length cells. There is no distinct effect of sample thickness on the peak shape distortion.

We also examined the effect of the sample thickness on the 2D-DQC spectra. A theoretical study on peak shape distortion in 2D photon echo spectra reported that optically thick samples can distort peak shapes in 2D echo spectra.[42] To check such effects on the 2D-DQC spectra, we measured the 2D spectra of samples that have the same optical densities (~0.3) but are contained in cuvettes of different thicknesses (1 mm versus 0.2 mm path length), as shown in Figure 5. The two spectra are not significantly different in their peak shapes, except for delicate changes in the overall peak shape. Most of all, the shift of the peaks from the diagonal, that is, Δ, is not affected by the sample thickness.

C. Effect of Solvent and Excitation Wavelength on the DQC Energy Shift. A series of measurements were carried out to investigate whether the measured signals, and particularly Δ, depend on solvent or excitation wavelength. The 2D-DQC spectra of Nile red were measured in four different solvents

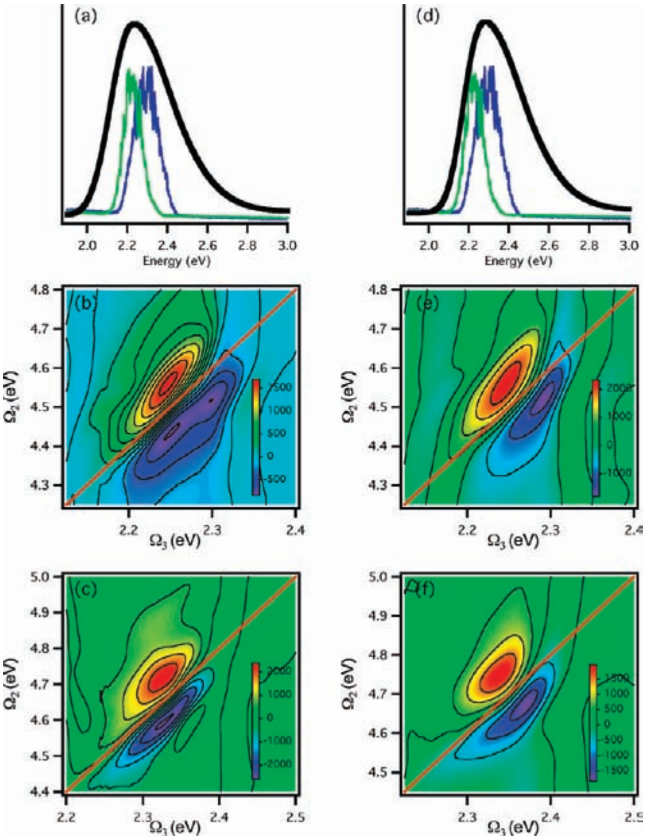

Figure 6. Solvent and excitation wavelength dependence of 2D-DQC spectra and electron correlation energy shift studied using the solvatochromic dye Nile red. The left column (a, b, c) corresponds to Nile red in ethanol and the right (d, e, f) to Nile red in dichloromethane. (a) Absorption spectrum (black line) of Nile red in ethanol plotted with experimental laser spectra centered at 2.30 eV (540 nm, blue line) and 2.23 eV (555 nm, green line). (b) Re 2D-DQC spectrum of Nile red in ethanol measured using the laser spectrum centered at 2.23 eV. (c) Re 2D-DQC spectrum of Nile red in ethanol measured using the laser spectrum centered at 2.30 eV. (d) Absorption spectrum (black line) of Nile red in dichloromethane with the same experimental laser spectra as (a). (e) Re 2D-DQC spectrum of Nile red in dichloromethane measured at 2.23 eV. (f) Re 2D-DQC spectrum of Nile red in dichloromethane measured using the laser spectrum centered at 2.30 eV. The black line in all of the 2D-DQC spectra corresponds to the diagonal $\Omega_2 = 2\Omega_3$.

(ethanol, dichloromethane, DMSO, and acetone) and at two different excitation wavelengths (2.23 and 2.30 eV). Representative results are shown in Figure 6. The study of solvent dependence is aimed at ascertaining whether the correlation energy is affected by a polarizable dielectric environment surrounding the dye molecule. Nile red is soluble in various solvents with different static dielectric constants (ε) and optical dielectric constants (n^2, where n is the refractive index). Significant solvatochromism is evident in the absorption spectra with the maximum peak of Nile red-shifted from 2.335 eV (531 nm) to 2.242 eV (553 nm) in these solvents, Table 1. In contrast to the solvatochromism effect exhibited in the absorption spectrum, the solvent dependence of the DQC energy shift Δ was found to be negligible, with a deviation of only ±6% between different solvents used in this work, as summarized in Table 1. Furthermore, the DQC energy shift was found to vary little when comparing the two different excitation wavelengths. However, the excitation wavelength seems to influence the amplitude ratio of positive and negative peaks, which can be ascribed to the effects of vibronic transitions as will be described later in this paper.

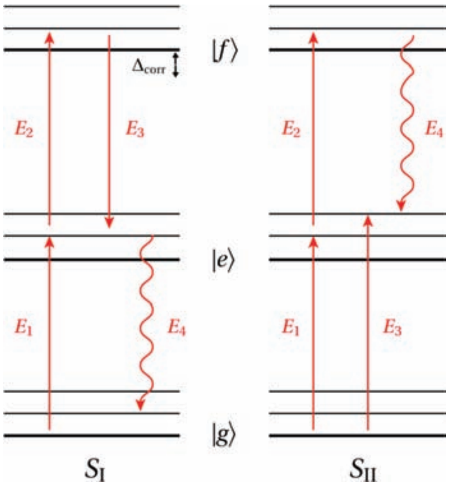

Figure 7. Quantum pathways of 2D-DQCS signal in a three-level system with vibronic transitions considered.

5. Vibronic Transitions in DQCS

In linear spectroscopy, like absorption and fluorescence, it is clear that vibronic transitions are measured, not purely electronic transitions. In that case, when we write $|g\rangle$ we really mean (in the Born−Oppenheimer approximation) the product function of the electronic ground state with the vibrational wave functions of the nuclei. The same is true for nonlinear spectroscopy, although the vibronic structure in 2D electronic spectroscopy is usually neglected. Here we consider the influence of vibronic transitions. To do that we sum over all vibronic transitions, not just purely electronic transitions between $|g\rangle$, $|e\rangle$, and $|f\rangle$, and modify, in the usual way (vide infra), the associated transition dipole strengths by their relative Franck−Condon factors.

In the systems we have studied experimentally there are only single $|e\rangle$ and $|f\rangle$ states in resonance with the excitation pulses. On the basis of this three-level electronic manifold, we illustrate in Figure 7 how vibronic transitions modify the resonances that contribute to the 2D-DQC signal. In contrast to consideration of only electronic states, each vibronic pathway is weighted by a product of Franck−Condon overlaps. A further difference is the introduction of vibrational levels in the ground state, yielding features at lower frequencies on the Ω_3 axis than anticipated

TABLE 1: Physical Parameters and DQC Energy Shift (Δ) of Solvatochromic Dye Nile Red

solvent	static dielectric constant (ε)	optical dielectric constant (n^2)	absorption maximum (eV)	center energy of excitation	DQC energy shift Δ (meV)
dichloromethane	8.51	2.029	2.305	2.23	62.1
dichloromethane	8.51	2.029	2.305	2.30	67.9
acetone	20.7	1.847	2.335	2.30	56.0
ethanol	24.35	1.853	2.258	2.23	70.1
ethanol	24.35	1.853	2.258	2.30	64.0
dimethyl sulfoxide (DMSO)	47.24	2.008	2.242	2.23	61.8

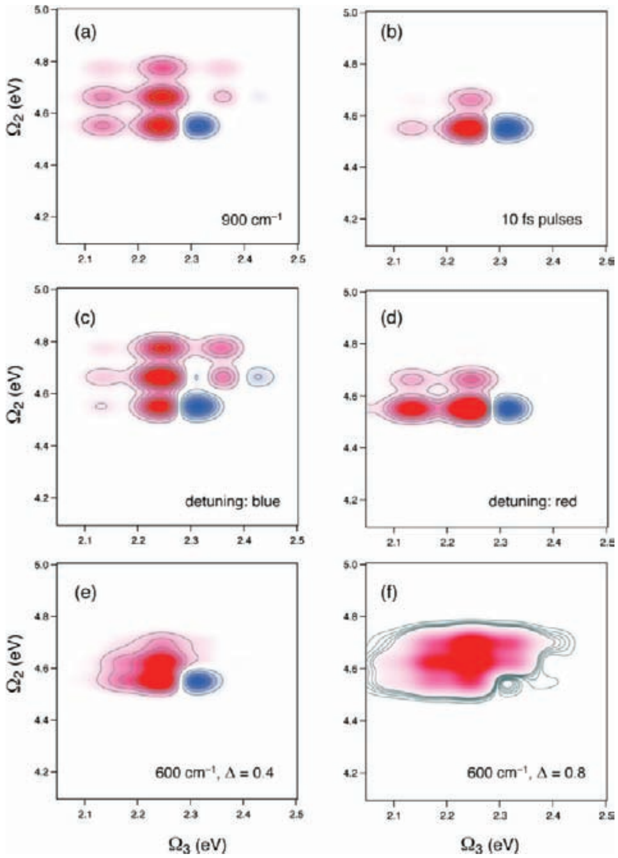

Figure 8. Simulation results of 2D-DQCS spectra with vibronic transitions.

by a purely electronic model. The vibronic transitions contribute differently in the denominators of the two signal pathways, producing more complicated interference effects. Nonetheless, as we describe below, in most cases the primary feature of the 2D-DQC signal turns out to be the interference of purely electronic resonances. Equation 1 is modified to include vibronic transitions as follows

$$S(\Omega_3, \Omega_2, t_1 = 0) = \sum_{e,e',f} \sum_{u_e,u_f,v_{e'},v_g} \frac{A\langle\chi(u_f)|\mu_{fe}|\chi(u_e)\rangle\langle\chi(u_e)|\mu_{eg}|\chi(u_g)\rangle}{\Omega_2 - (\omega_{fg} + u_f - u_e) + i\gamma} \times \left[\frac{A'_{\mathrm{I}}\langle\chi(v_g)|\mu_{ge'}|\chi(v_{e'})\rangle\langle\chi(v_{e'})|\mu_{e'f}|\chi(u_f)\rangle}{\Omega_3 - (\omega_{e'g} + v_{e'} - v_g) + i\gamma} - \frac{A'_{\mathrm{II}}\langle\chi(u_g)|\mu_{ge'}|\chi(v_{e'})\rangle\langle\chi(v_{e'})|\mu_{e'f}|\chi(u_f)\rangle}{\Omega_3 - (\omega_{fe'} + u_f - v_{e'}) + i\gamma}\right] \quad (7)$$

where u_e and u_f are vibrational frequencies in the $|e\rangle$ and $|f\rangle$ states, respectively, excited by the first two pulses during excitation of the double-quantum coherence. The u_g are the frequencies in the initial, thermalized, ground state of the molecule with population weighted by the appropriate Boltzmann factor. The $v_{e'}$ and v_g are vibrational frequencies in the $|e'\rangle$ and $|g\rangle$ states, respectively, accessed by the third laser pulse and radiation of the signal. The vibrational wave function corresponding to each frequency v is labeled $\chi(v)$.

For the present purposes we assumed no Duschinsky rotation and equal ground and excited state frequencies so that the Franck–Condon overlaps in eq 7 were modeled by the simple expressions collected in eqs 8.[43] These approximations can easily be relaxed, for example, to use 2D-DQC to measure frequencies in ground versus excited states.

$$\langle 0|0\rangle = \sqrt{2}\exp(-\Delta_v^{\,2}/2) \quad (8a)$$

$$\langle 0|m\rangle = \langle m|0\rangle = [\exp(-\Delta_v^{\,2}/2)(\Delta_v^{\,2}/2)^m/m!]^{1/2} \quad (8b)$$

$$\langle m|n\rangle = \langle 0|0\rangle^{-1}\sum_{k=0}^{\min(m,n)}\frac{1}{k!}\left[\frac{m!n!}{(m-k)!(n-k)!}\right]^{1/2} \times \langle m-k|0\rangle\langle 0|n-k\rangle \quad (8c)$$

Here $|m\rangle$ denotes m quanta of the mode and Δ_v is the dimensionless displacement of this mode between ground and single-quantum state (not to be confused with the DQC energy shift Δ). We assume here that the mode displacements between ground and single-quantum states are equivalent to those between single-quantum states and double-quantum states, which seems a reasonable first approximation given the common symmetry of ground and double-quantum states.

Finite pulse duration was modeled by the A factors, which were set equal to unity in the original theoretical work[13,14] to ignore pulse duration effects. We used the following expressions[13,44]

$$A = \varepsilon_1[\omega_1 - (\omega_{eg} + u_e - u_g)]\varepsilon_2[\omega_2 - (\omega_{fe} + u_f - u_e)]\varepsilon_3^*[(\omega_{fe'} + u_f - v_{e'}) - \omega_3] \quad (9a)$$

$$A'_{\mathrm{I}} = \varepsilon_4^*[(\omega_{e'g} + v_{e'} - v_g) - \omega_4] \quad (9b)$$

$$A'_{\mathrm{II}} = \varepsilon_4^*[(\omega_{e'g} + v_{e'} - u_g) - \omega_4] \quad (9c)$$

where ω_j is the carrier frequency of laser pulse j and we have assumed the laser pulse envelopes $\varepsilon_j[\omega]$ are Gaussian and transform-limited.

6. Simulation Results and Discussion

In Figure 8 we report simulations of 2D-DQC signals. In Figure 8a–d we plot calculations for a single mode with a frequency of 900 cm^{-1} and a displacement of 0.4. Figure 8a shows results for a calculation with infinitely short laser pulses, and the pattern of vibronic features is clearly seen. Features at energies on the Ω_3 axis corresponding to excitations below the electronic energy gap are evident. They result from signal pathway S_{I} where the radiated signal de-excitates $|e\rangle$ to a vibrational excitation in $|g\rangle$. The peaks at higher energy along the Ω_2 axis result from excitation of vibrational modes in $|f\rangle$, which generate signals dominantly in the S_{I} term because those same vibrational excitations can be preserved in the downward pathway $|f\rangle \rightarrow |e\rangle \rightarrow |g\rangle$. The signal S_{II}, on the other hand, radiates from $|f\rangle\langle e|$ to $|e\rangle\langle e|$. Pulse 3 prepares the $|f\rangle\langle e|$ coherence by exciting from $\langle g|$ to $\langle e|$, meaning that vibrations in the electronic ground state do not contribute at all to S_{II} (unless thermally occupied). The result is that the positive signal dominates over the negative signal when the electronic transitions couple to vibrational modes of frequency greater than thermal energies.

Figure 8b shows a calculation similar to that shown in Figure 8a, but with consideration of finite pulse duration, and hence excitation bandwidth. Here the pulses are centered at 2.246 eV

(552 nm), precisely on resonance with ω_{eg}, and are considered to be 10 fs in duration (full width at half-maximum of the electric field envelope). As a result of the nonlinear intensity dependence of the signal and the frequency-dependent excitation intensity, signal features are obscured compared to Figure 8a. In panels c and d of Figure 8 we plot examples of laser pulse detuning from blue excitation at 2.4 eV (516 nm) to red excitation at 2.1 eV (590 nm). Both these examples assume 6 fs duration pulses. Red-edge excitation therefore provides signals that are less congested with vibronic features and is therefore the preferred method for estimation of the electronic correlation energy shift.

In panels e and f of Figure 8 we report calculations for a single mode with a frequency of 600 cm^{-1} and a displacement of 0.4 versus 0.8 (6 fs pulses centered on the ω_{eg} resonance). Comparing the simulations for the 900 cm^{-1} vibration, Figure 8a,b, with those for a 600 cm^{-1} vibration, Figure 8e,f, it is apparent that higher frequency modes, provided they are sufficiently coupled to the electronic transition, perturb the shape of the signal more dramatically than low frequency modes. It is also evident that larger displacements bias the signal more to the positive (S_I) term. It can be imagined that when several modes are strongly coupled to the electronic transitions the 2D-DQC spectra will show many features in addition to the purely electronic response that yields the electron correlation energy offset.

Analysis of vibronic progressions in resonance Raman data and related experiments such as hyper-Raman processes have proven to yield valuable insights into the structure of molecules in solution as well as ultrafast structural changes.[43,45−47] Our analysis suggests that related information is contained in the 2D-DQC data. This may provide routes in the future for correlating structure and structural dynamics with the reorganization (mean-field) and correlation of electronic motions.

In Figure 9a,b, we plot experimental data for the model chromophore Nile blue (dilute solution in ethanol recorded at 294 K). The absolute value data show that the positive peak dominates the measured signal, which is partly explained from our calculations by the greater number of signal-generating pathways for S_I compared to S_II when high-frequency vibrations are considered. The negative signal feature in Figure 9b at $\Omega_3 \sim 1.87$ eV cannot be assigned. The peak is only occasionally seen in experiments, and we believe that it is an artifact, possibly due to the solvent background or fluorescence. In Figure 9c we report calculations of the 2D-DQC signal that includes correlated static disorder in the transition frequencies (calculated as we have described previously[15]) and three important high-frequency modes. Modes representative of the experimental results of Lawless and Mathies[48] were included in the calculation: 400 cm^{-1} ($\Delta_v = 0.1$), 600 cm^{-1} ($\Delta_v = 0.7$), and 900 cm^{-1} ($\Delta_v = 0.22$). The contribution of the 600 cm^{-1} mode was reduced compared to the others to account for the fact that we have not counted many other vibrations with small displacements. Overall, the simulated signal captures many of the qualitative features in the experimental data.

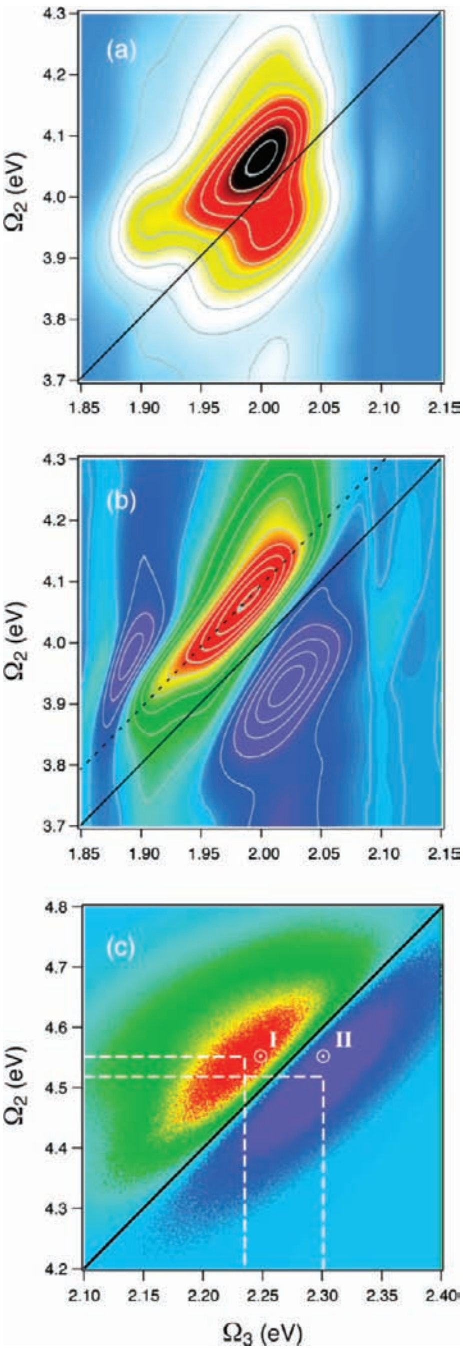

Figure 9. Comparison of experimental and simulated 2D-DQC spectra. (a) Absolute value and (b) real part of experimentally measured 2D-DQC spectrum of Nile blue. (c) Real part of simulated 2D-DQC spectrum with an electronic transition with the transition frequency of 2.25 eV.

The peak and trough of the calculated signal contributions, S_I and S_II, respectively, are indicated by the dashed lines. Similarly to the experimental results, the S_II feature peaks slightly below S_I on the Ω_2 axis. The correct positions of the electronic resonances ($\Omega_2 = \omega_{fg}$, $\Omega_3 = \omega_{eg})_\text{I}$ and ($\Omega_2 = \omega_{fg}$, $\Omega_3 = \omega_{fe})_\text{II}$ are indicated by the points labeled I and II. The calculated peak (red) lies at the correct $\Omega_2 = \omega_{fg}$ double-quantum energy but is red-shifted on the Ω_3-axis ($\Omega_3 < \omega_{eg}$) owing to distortion of the band by vibronic features. On the other hand, the trough (violet) is located at $\Omega_2 < \omega_{fg}$, and $\Omega_3 = \omega_{fe}$ as a result of interference with the more intense, overlapping S_I signal. That was confirmed by simulating the signals in isolation from each other. As a consequence of the peak/trough shifts, analysis of these calculated data overestimates the correlation energy shift, defined as $\Delta_\text{corr} = \omega_{fe} - \omega_{eg}$, by almost a factor of 2. However, if we take the peak of S_I to give ω_{fg} and the trough of S_II to give ω_{fe}, then we find that $\Delta_\text{corr} = 2\omega_{fe} - \omega_{fg} = +60$ meV, precisely as input into the calculation.

7. A Note on the Meaning of Δ

Single and double quantum transitions are well-known in vibrational spectroscopy as the fundamental and overtone

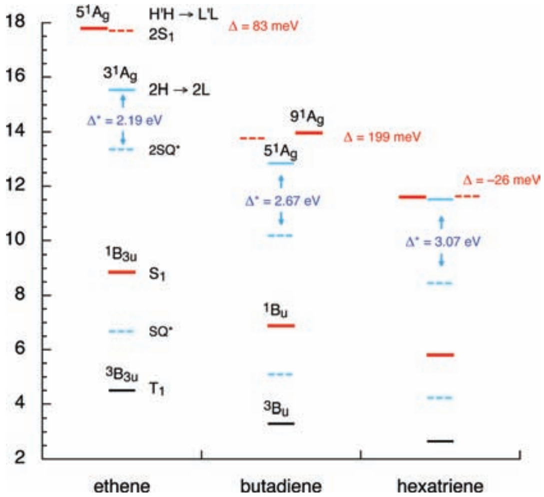

Figure 10. Electronic transition energies (eV) relevant to the discussion about DQCS calculated using the EOM-CCSD/cc-pVDZ level of theory. See text for details.

frequencies, respectively. Owing to anharmonicity, the overtone is found at a frequency less than twice the fundamental. That is, Δ is negative. That is in contrast to the results reported in the present paper where we have studied "electronic oscillators".[49,50] The electronic oscillator problem is considerably more complicated than vibrational oscillators because electronic transition frequencies are determined by the many-body response of electrons in a molecule.[19,51−53] As indicated earlier in this paper, the interpretation of DQCS is challenging, and further work is needed to elucidate how we can learn quantitatively about electron correlation from these measurements. To show what we mean by this statement, the results of high-quality quantum chemical calculations on model polyenes will be briefly described.

Optimized geometries of ethane, butadiene, and hexatriene were taken from the literature.[54] Calculations of excited states were performed using various methods and basis sets. Here we report results obtained at the EOM-CCSD level of theory using the cc-pVDZ basis set.[55−58] Calculations were carried out using the QChem program.[59] To obtain the double-quanta states many highly excited states needed to be calculated, for example, the first 48 states in the case of butadiene. Only the electronic states relevant to the discussion below are collected in Figure 10.

The electronic states, and their transition energies from the ground state, that are directly relevant to the DQCS experiment (as we have performed it) are plotted in red in Figure 10. The S_1 state is $|e\rangle$, the lowest allowed electronic transition from $|g\rangle$. The dashed red line is not a calculated state but marks twice the energy of the S_1 transition. The nearest electronic state to this point that has the correct symmetry to be photoexcited from S_1 (a singlet ^1A_g state) corresponds to $|f\rangle$. We found it to have some double highest occupied (HOMO) to lowest unoccupied molecular orbital (LUMO) character, 2H → 2 L, but it is mainly composed of a double excitation from two different HOMOs to two different LUMOs, H′H → L′L. The values for Δ that we report in the previous sections of the paper correspond to the energy difference between the H′H → L′L transition and the energy $2S_1$. It is seen in Figure 10 that there is no apparent trend in this Δ through the series of three polyenes.

When describing the goal of DQCS, we stated that it is desirable to measure how the energy of a H → L transition is modified by the reorganization of electrons in the molecule caused by a preceding H → L transition. As mentioned already, a difficulty in addressing this question is that the exchange interaction involving the HOMO and LUMO electrons needs to be accounted for; it strongly influences the single-quantum transition energy but not that of the double-quantum transition. The blue markers in Figure 10 illustrate how to obtain this correlation energy, labeled Δ*.

To compensate for the exchange interaction, the lowest energy singlet and triplet excited state energies, S_1 and T_1, were calculated and an exchange-corrected single-quantum transition energy SQ* was found as $[S_1 + T_1]/2$. Twice the energy of SQ* is labeled 2SQ*, which is compared to the calculated energy of the 2H → 2L transition, that is, the "true" double-quantum transition, to give Δ*. As expected for strongly correlated systems, Δ* is large. It is found to increase systematically through the ethane, butadiene, hexatriene series.

The brief analysis presented in this section of the paper suggests that the ideal description of the DQCS experiment and the practical implementation measure different quantities in the case of strongly correlated systems. Nonetheless, the potential of the technique is evident and this will motivate future development.

8. Conclusions

We demonstrated that 2D-DQCS maps out the energies and correlations of single and double excited states in a two-dimensional spectrum consisting of one-quantum and two-quantum transition frequencies, as predicted by theory.[13,14] In particular, the narrow peak width in the antidiagonal direction allows one to achieve higher spectral resolution than that obtained by traditional linear and two-photon absorption spectroscopies. As a result of the interaction between single excitations, the double-quantum resonances observed in the measured 2D-DQC spectra are substantially shifted compared to the case of noninteracting excitations, by the amount of tens of millielectronvolts for the transitions of the molecular chromophores examined in this work. We also examined the effect of excitation bandwidth and cell thickness on the measured 2D-DQC spectra. In addition, we found that neither the solvent environment nor the excitation wavelength has a significant effect on the quantum correlation energy (assuming approximately resonant conditions). However, shifts in the excitation wavelength were found to change the relative intensities of the positive and negative peaks in the Re spectra as explained by vibrational contributions.

Simulations of the 2D-DQC spectra suggest that consideration of the vibronic structure helps to explain the asymmetry and, in general, complex shape of the experimental 2D-DQCS data. In particular we were able to explain, first, that the dominant positive and negative peaks in the experimental data are skewed relative to each other such that the negative peak lies lower on the Ω_2 axis than the positive peak. The experimental data are more distorted than the simulations predict, and further experimental study is needed to investigate this issue. Second, the negative peak is typically found to be weaker than the positive peak. This was explained by the observation that there are more signal-generating pathways in S_{I} relative to S_{II} when high-frequency vibrations couple to the excitations because the S_{I} pathway accesses de-excitation to the ground state vibrational manifold. The S_{II} pathway has a more limited signal resonance between a vibrationally excited $\langle f|$ and vibrational excitations in $\langle e|$.

The correlated motions of electrons in molecules are very significant, especially in excited electronic states, and may one day be harnessed to expose new modes of chemical reactivity.

The overall goal of our continuing work is to begin to elucidate insights into chemistry beyond mean-field approximations. To this end, we described the application and interpretation of a coherent two-dimensional electronic spectroscopy that measures changes in the electronic interactions among electrons and their many-body correlated response to optical excitation. It was found that the method is useful, but the challenge of interpretation of the results remains.

Acknowledgment. The Natural Sciences and Engineering Research Council of Canada is gratefully acknowledged for the support of this research. G.D.S. acknowledges the support of an NSERC E. W. R. Steacie Memorial Fellowship.

Supporting Information Available: Further details of the data processing. This material is available free of charge via the Internet at http://pubs.acs.org.

References and Notes

(1) Hamm, P.; Lim, M.; Hochstrasser, R. M. *J. Phys. Chem. B* **1998**, *102*, 6123.

(2) Asplund, M. C.; Zanni, M. T.; Hochstrasser, R. M. *Proc. Natl. Acad. Sci. U.S.A.* **2000**, *97*, 8219.

(3) Golonzka, O.; Khalil, M.; Demirdoven, N.; Tokmakoff, A. *Phys. Rev. Lett.* **2001**, *86*, 2154.

(4) Zheng, J.; Kwak, K.; Asbury, J.; Chen, X.; Piletic, I. R.; Fayer, M. D. *Science* **2005**, *309*, 1338.

(5) Ding, F.; Fulmer, E. C.; Zanni, M. T. *J. Chem. Phys.* **2005**, *123*, 094502.

(6) Mukamel, S. *Annu. Rev. Phys. Chem.* **2000**, *51*, 691.

(7) Hybl, J. D.; Ferro, A. A.; Jonas, D. M. *J. Chem. Phys.* **2001**, *115*, 6606.

(8) Jonas, D. M. *Annu. Rev. Phys. Chem.* **2003**, *54*, 425.

(9) Brixner, T.; Mancal, T.; Stiopkin, I. V.; Fleming, G. R. *J. Chem. Phys.* **2004**, *121*, 4221.

(10) Brixner, T.; Stenger, J.; Vaswani, H. M.; Cho, M.; Blankenship, R. E.; Fleming, G. R. *Nature* **2005**, *434*, 625.

(11) Cho, M. *Chem. Rev.* **2008**, *108*, 1331.

(12) Ernst, R. R.; Bodenhausen, G.; Wokaun, A. *Principles of Nuclear Magnetic Resonances in One and Two Dimensions*; Clarendon Press: Oxford, 1987.

(13) Li, Z.; Abramavicius, D.; Mukamel, S. *J. Am. Chem. Soc.* **2008**, *130*, 3509.

(14) Mukamel, S.; Oszwaldowski, R.; Yang, L. *J. Chem. Phys.* **2007**, *127*, 221105.

(15) Kim, J.; Mukamel, S.; Scholes, G. D. *Acc. Chem. Res.* **2009**, *42*, 1375.

(16) Mukamel, S.; Abramavicius, D.; Yang, L.; Zhuang, W.; Schweigert, I. V.; Voronine, D. V. *Acc. Chem. Res.* **2009**, *42*, 553.

(17) Ikura, M.; Hikichi, K. *J. Am. Chem. Soc.* **1984**, *106*, 4275.

(18) Fulmer, E. C.; Mukherjee, P.; Krummel, A. T.; Zanni, M. T. *J. Chem. Phys.* **2004**, *120*, 8067.

(19) Wilson, S. *Electron Correlation in Molecules*; Oxford University Press: Oxford, 1984.

(20) Bogdan, A.; Downer, M.; Bloembergen, N. *Phys. Rev. A* **1981**, *24*, 623.

(21) Andrews, J. R.; Hochstrasser, R. M. *Chem. Phys. Lett.* **1981**, *82*, 381.

(22) Moran, A. M.; Park, S.; Scherer, N. F. *Chem. Phys.* **2007**, *341*, 344.

(23) Venkatramani, R.; Mukamel, S. *J. Phys. Chem. B* **2005**, *109*, 8132.

(24) Ehara, M.; Ishida, M.; Toyota, K.; Nakatsuji, H. SAC-CI general-R method: Theory and applications to the multi-electron processes. In *Reviews in Modern Quantum Chemistry*; Sen, K. D. , Ed.; World Scientific: Singapore, 2002; pp 293.

(25) Frisch, M. J.; Trucks, G. W.; Schlegel, H. B.; Scuseria, G. E.; Robb, M. A.; Cheeseman, J. R.; Montgomery, J. A., Jr.; Vreven, T.; Kudin, K. N.; Burant, J. C.; Millam, J. M.; Iyengar, S. S.; Tomasi, J.; Barone, V.; Mennucci, B.; Cossi, M.; Scalmani, G.; Rega, N.; Petersson, G. A.; Nakatsuji, H.; Hada, M.; Ehara, M.; Toyota, K.; Fukuda, R.; Hasegawa, J.; Ishida, M.; Nakajima, T.; Honda, Y.; Kitao, O.; Nakai, H.; Klene, M.; Li, X.; Knox, J. E.; Hratchian, H. P.; Cross, J. B.; Bakken, V.; Adamo, C.; Jaramillo, J.; Gomperts, R.; Stratmann, R. E.; Yazyev, O.; Austin, A. J.; Cammi, R.; Pomelli, C.; Ochterski, J. W.; Ayala, P. Y.; Morokuma, K.; Voth, G. A.; Salvador, P.; Dannenberg, J. J.; Zakrzewski, V. G.; Dapprich, S.; Daniels, A. D.; Strain, M. C.; Farkas, O.; Malick, D. K.; Rabuck, A. D.; Raghavachari, K.; Foresman, J. B.; Ortiz, J. V.; Cui, Q.; Baboul, A. G.; Clifford, S.; Cioslowski, J.; Stefanov, B. B.; Liu, G.; Liashenko, A.; Piskorz, P.; Komaromi, I.; Martin, R. L.; Fox, D. J.; Keith, T.; Al-Laham, M. A.; Peng, C. Y.; Nanayakkara, A.; Challacombe, M.; Gill, P. M. W.; Johnson, B.; Chen, W.; Wong, M. W.; Gonzalez, C.; Pople, J. A. *Gaussian 03, Revision D.01*; Gaussian, Inc.: Wallingford, CT, 2004.

(26) Saha, B.; Ehara, M.; Nakatsuji, H. *J. Chem. Phys.* **2006**, *125*, 014316.

(27) Salvador, M. R.; Hines, M. A.; Scholes, G. D. *J. Chem. Phys.* **2003**, *118*, 9380.

(28) Goodno, G. D.; Dadusc, G.; Miller, R. J. D. *J. Opt. Soc. Am. B* **1998**, *15*, 1791.

(29) Collini, E.; Scholes, G. D. *J. Phys. Chem. A* **2009**, *113*, 4223.

(30) Collini, E.; Scholes, G. D. *Science* **2009**, *323*, 369.

(31) Lepetit, L.; Joffre, M. *Opt. Lett.* **1996**, *21*, 564.

(32) Gallagher, S. M.; Albrecht, A. W.; Hybl, J. D.; Landin, B. L.; Rajaram, B.; Jonas, D. M. *J. Opt. Soc. Am. B* **1998**, *15*, 2338.

(33) Dorrer, C.; Belabas, N.; Likforman, J. P.; Joffre, M. *J. Opt. Soc. Am. B* **2000**, *17*, 1795.

(34) Leo, K.; Wegener, M.; Shah, J.; Chemla, D. S.; Gobel, E. O.; Damen, T. C.; Schmitt-Rink, S.; Schafer, W. *Phys. Rev. Lett.* **1990**, *65*, 1340.

(35) Wang, H.; Ferrio, K. B.; Steel, D. G.; Berman, P. R.; Hu, Y. Z.; Binder, R.; Koch, S. W. *Phys. Rev. A* **1994**, *49*, R1551.

(36) Chemla, D. S.; Shah, J. *Proc. Natl. Acad. Sci. U.S.A.* **2000**, *97*, 2437.

(37) Chemla, D. S.; Shah, J. *Nature* **2001**, *411*, 549.

(38) Mukamel, S.; Tortschanoff, A. *Chem. Phys. Lett.* **2002**, *357*, 327.

(39) Zhang, W. M.; Chernyak, V.; Mukamel, S. *J. Chem. Phys.* **1999**, *110*, 5011.

(40) Hybl, J. D.; Christophe, Y.; Jonas, D. M. *Chem. Phys.* **2001**, *266*, 295.

(41) Abramavicius, D.; Voronine, D. V.; Mukamel, S. *Proc. Natl. Acad. Sci. U.S.A.* **2008**, *105*, 8525.

(42) Yetzbacher, M. K.; Belabas, N.; Kitney, K. A.; Jonas, D. M. *J. Chem. Phys.* **2007**, *126*, 044511.

(43) Myers, A. B.; Mathies, R. A. *J. Chem. Phys.* **1984**, *81*, 1552.

(44) Schweigert, I. V.; Mukamel, S. *Phys. Rev. A* **2008**, *77*, 033802.

(45) Lee, S.-Y.; Heller, E. J. *J. Chem. Phys.* **1979**, *71*, 4777.

(46) Myers, A. B. *J. Opt. Soc. B* **1990**, *7*, 1665.

(47) Kelley, A. M. *J. Phys. Chem. A* **2008**, *112*, 11975.

(48) Lawless, M. K.; Mathies, R. A. *J. Chem. Phys.* **1992**, *96*, 8037.

(49) Mukamel, S.; Tretiak, S.; Wagersreiter, T.; Chernyak, V. *Science* **1997**, *277*, 781.

(50) Tretiak, S.; Mukamel, S. *Chem. Rev.* **2002**, *102*, 3171.

(51) Head-Gordon, M.; Lee, T. J. Single reference coupled cluster and perturbation theories of electronic excitation energies. In *Recent Advances in Coupled-Cluster Methods*; Bartlett, R. J. , Ed.; World Scientific: Singapore, 1997; pp 221.

(52) Schirmer, J. *Phys. Rev. A* **1982**, *26*, 2395.

(53) Koch, H.; Jørgensen, P. *J. Chem. Phys.* **1990**, *93*, 3333.

(54) Catalán, J.; de Paz, J. L. G. *J. Chem. Phys.* **2004**, *120*, 1864.

(55) Bartlett, R. J. *Annu. Rev. Phys. Chem.* **1981**, *32*, 359.

(56) Krylov, A. I. *Annu. Rev. Phys. Chem.* **2008**, *59*, 433.

(57) Stanton, J. F.; Bartlett, R. J. *J. Chem. Phys.* **1993**, *98*, 7029.

(58) Levchenko, S. V.; Krylov, A. I. *J. Chem. Phys.* **2004**, *120*, 175.

(59) Shao, Y.; Molnar, L. F.; Jung, Y.; Kussmann, J.; Ochsenfeld, C.; Brown, S. T.; Gilbert, A. T. B.; Slipchenko, L. V.; Levchenko, S. V.; O'Neill, D. P.; DiStasio, R. A.; Lochan, R. C.; Wang, T.; Beran, G. J. O.; Besley, N. A.; Herbert, J. M.; Lin, C. Y.; Van Voorhis, T.; Chien, S. H.; Sodt, A.; Steele, R. P.; Rassolov, V. A.; Maslen, P. E.; Korambath, P. P.; Adamson, R. D.; Austin, B.; Baker, J.; Byrd, E. F. C.; Dachsel, H.; Doerksen, R. J.; Dreuw, A.; Dunietz, B. D.; Dutoi, A. D.; Furlani, T. R.; Gwaltney, S. R.; Heyden, A.; Hirata, S.; Hsu, C.-P.; Kedziora, G.; Khalliulin, R. Z.; Klunzinger, P.; Lee, A. M.; Lee, M. S.; Liang, W.; Lotan, I.; Nair, N.; Peters, B.; Proynov, E. I.; Pieniazek, P. A.; Rhee, Y. M.; Ritchie, J.; Rosta, E.; Sherrill, C. D.; Simmonett, A. C.; Subotnik, J. E.; Woodcock, H. L.; Zhang, W.; Bell, A. T.; Chakraborty, A. K.; Chipman, D. M.; Keil, F. J.; Warshel, A.; Hehre, W. J.; Schaefer, H. F.; Kong, J.; Krylov, A. I.; Gill, P. M. W.; Head-Gordon, M *Phys. Chem. Chem. Phys.* **2006**, *8*, 3172.

JP907327M